

PROPERTIES OF UMBRAL DOTS FROM STRAY LIGHT CORRECTED *Hinode* FILTERGRAMS

ROHAN E. LOUIS^{1,2}, SHIBU K. MATHEW², LUIS R. BELLOT RUBIO³, KIYOSHI ICHIMOTO⁴, B. RAVINDRA⁵ AND A. RAJA BAYANNA²

Draft version August 18, 2018

ABSTRACT

High resolution blue continuum filtergrams from *Hinode* are employed to study the umbral fine structure of a regular unipolar sunspot. The removal of scattered light from the images increases the *rms* contrast by a factor of 1.45 on average. Improvement in image contrast renders identification of short filamentary structures resembling penumbrae that are well separated from the umbra-penumbra boundary and comprise bright filaments/grains flanking dark filaments. Such fine structures were recently detected from ground based telescopes and have now been observed with *Hinode*. A multi-level tracking algorithm was used to identify umbral dots in both the uncorrected and corrected images and to track them in time. The distribution of the values describing the photometric and geometric properties of umbral dots are more easily affected by the presence of stray light while it is less severe in the case of kinematic properties. Statistically, umbral dots exhibit a peak intensity, effective diameter, lifetime, horizontal speed and a trajectory length of $0.29I_{QS}$, 272 km, 8.4 min, 0.45 km s^{-1} and 221 km respectively. The 2 hr 20 min time sequence depicts several locations where umbral dots tend to appear and disappear repeatedly with various time intervals. The correction for scattered light in the *Hinode* filtergrams facilitates photometry of umbral fine structure which can be related to results obtained from larger telescopes and numerical simulations.

Subject headings: Sun sunspots—umbra—techniques photometric

1. INTRODUCTION

The dark umbral background is populated by small, bright features called umbral dots (UDs). The size of UD ranges from $0''.8$ to about $0''.2$ based on previous studies by Sobotka et al. (1997a) and Tritschler & Schmidt (2002), while a recent work by Riethmüller et al. (2008b) shows that the size distribution of UD diameters is a maximum around $0''.3$ or 225 km, suggesting that most of the UD are spatially resolved. Sobotka et al. (1997a) also observed that the larger, long-lived UD are seen in regions of enhanced umbral background intensity. The darkest parts of the umbral core, referred to as dark nuclei, are often devoid of UD. Based on their relative location, UD can be classified as “central” and “peripheral”. While the former are seen in the inner regions of the umbra, the latter dominate the umbra-penumbra boundary. Peripheral UD are usually brighter than the central ones. The intensity of UD ranges from about 0.2 to 0.7 times the normal photospheric intensity at visible wavelengths. The typical speeds of UD are $\approx 400 \text{ m s}^{-1}$ (Sobotka et al. 1997b; Kitai et al. 2007; Riethmüller et al. 2008b; Sobotka & Puschmann 2009). Most mobile UD emerge near the umbra-penumbra boundary and move towards the center of the umbra (Riethmüller et al. 2008b) with speeds of 700

m s^{-1} . UD do not have a typical lifetime, with values ranging from 10 min to 2.5 min (Sobotka et al. 1997a; Riethmüller et al. 2008b; Hamedivafa 2011; Watanabe et al. 2009). The spread in the values arises from the manner in which UD can be grouped based on their size, lifetime and spatial location.

Parker (1979) proposed that UD are manifestations of hot non-magnetized plasma pushing its way in the gappy umbral field. While the detection of such weak fields in the umbra remains elusive, observations indicate a reduction of 300-500 G in UD (Schmidt & Balthasar et al. 1994; Socas-Navarro et al. 2004) with the contrasted ones residing in locations where the magnetic field is $\approx 2000 \text{ G}$ and is inclined more than 30° (Watanabe et al. 2009). Central and peripheral UD exhibit an enhancement in temperature of 550 K and 570 K respectively (Riethmüller et al. 2008a). The measurements of Doppler velocities in UD show that peripheral UD have an upflow of $\approx 0.4\text{-}0.8 \text{ km s}^{-1}$ (Rimmele 2004; Riethmüller et al. 2008a; Sobotka & Jurcak 2009a). Central UD on the other hand exhibit very weak downflows (Sobotka & Puschmann 2009) while Hartkorn & Rimmele (2003) detected downflows of upto 0.3 km s^{-1} . Ortiz et al. (2010) reported downflows at the edge of UD measuring 400 to 1000 m s^{-1} at a spatial resolution of $0''.14$. 3D MHD simulations of Schüssler & Vögler (2006), which model UD as narrow upflowing plumes in regions of intense magnetic fields, predicted a central dark lane in UD which was subsequently verified from high resolution ground based observations (Rimmele 2008; Sobotka & Puschmann 2009; Ortiz et al. 2010) as well as from space (Bharti et al. 2007). Recent observations from the 1.6 m NST indicate that UD are not perfectly circular but possess a mean eccentricity of 0.74 in the photosphere (Kilcik et al. 2012).

Electronic address: rlouis@aip.de

¹ Presently at Leibniz-Institut für Astrophysik Potsdam (AIP), An der Sternwarte 16, 14482 Potsdam, Germany

² Udaipur Solar Observatory, Physical Research Laboratory, Dewali, Badi Road, Udaipur, Rajasthan - 313004, India

³ Instituto de Astrofísica de Andalucía (CSIC), Apartado de Correos 3004, 18080 Granada, Spain

⁴ Kwasan and Hida Observatories, Kyoto University, Yamashina-ku, Kyoto 607-8417, Japan

⁵ Indian Institute of Astrophysics, II Block, Koramangla, Bangalore - 560 034, India

The extent to which UD's can be resolved depends on the spatial resolution which is presently $0''.14$ (Sobotka & Puschmann 2009; Ortiz et al. 2010) for a 1 m ground based telescope at 450 nm. This has been made possible with the aid of adaptive optics and post-processing techniques to minimize the contribution from “seeing”. On the other hand, *Hinode* (Kosugi et al. 2007) with a 50 cm aperture in space has a resolution of $0''.23$ at the same wavelength which can operate for long periods in the absence of the Earth’s atmospheric turbulence. Furthermore, since UD's are present in the darkest regions of sunspots, contamination by stray light can strongly influence photometric investigation of these structures. The motivation of this paper is to study the influence of stray light on the properties of UD's using *Hinode* data and how its removal compares with existing high resolution ground-based observations as well as numerical simulations. This exercise has been done taking into account the trade off between marginally coarser spatial resolution and the uninterrupted “seeing-free” time sequence between *Hinode* and its 1 m ground based counterpart. The rest of the paper is organized as follows. The observations are described in Section 2 and the results are presented in Section 3. In Section 4 we summarize our findings and discuss their implications.

2. OBSERVATIONS AND DATA PROCESSING

We utilize high resolution blue continuum filtergrams of the sunspot in NOAA AR 10944 acquired by the BFI (Broadband Filter Imager) of the SOT (Solar Optical Telescope; Tsuneta et al. 2008), on board *Hinode* from 00:14 - 02:34 UT on March 1, 2007. The sunspot was located very close to disc center (N0.7W4) at a heliocentric angle of $\Theta = 4^\circ$. The 1024×512 filtergrams had a pixel sampling of $0''.054$ and were taken at a cadence of 6 s with an exposure time of 102 ms. Initial processing of Level-0 data to Level-1 included dark correction, flat fielding and removal of bad pixels, and was carried out using the “*fg-prep*” routine in SolarSoft. The images were subsequently co-aligned using a 2D cross correlation routine.

In order to reduce the noise in the dark regions of the umbra, four successive filtergrams were added to yield a sequence of 326 images with a cadence of ~ 26 s. The averaging was carried out to keep the temporal resolution identical to the analysis of Watanabe et al. (2009) who had previously studied the same AR with the above data set. Applying the running average to the filtergrams leads to a reduction of power especially in the high spatial frequency domain as shown in the top panel of Figure 1 which depicts the azimuthally averaged power spectrum. The bottom panel of Figure 1 illustrates the difference in power between the single and mean image as a function of the spatial scale. Since the power is proportional to the square of the intensity, the relative intensity difference between the images varies from 2% to 5% for spatial scales of $0''.2$ and $0''.5$, respectively. This implies that averaging successive filtergrams should not significantly affect the detection of small scale structures within the umbra. We estimate the intensity fluctuations in the umbra to be 1.5% of the quiet Sun (QS) intensity. This value corresponds to three times the standard deviation of a small region in the umbral dark core. Averaging the filtergrams reduces the noise by $\approx 6\%$.

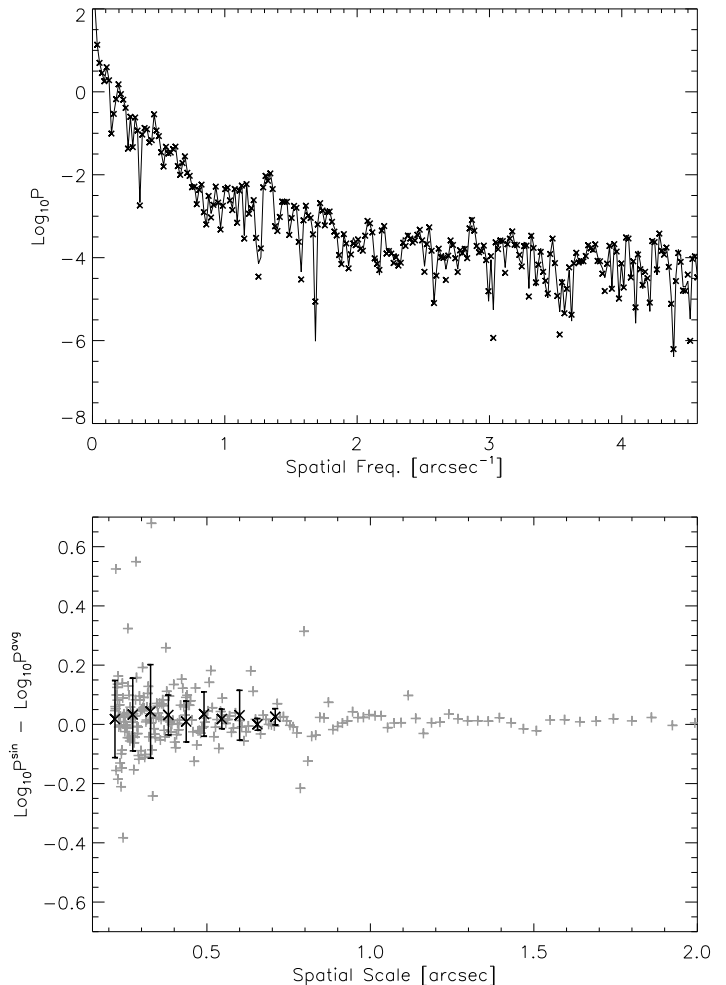


Fig. 1.— **Top:** Azimuthally averaged power spectra of single (solid line) and average of 4 blue continuum filtergrams (cross symbol). **Bottom:** Difference in power spectra of a single and average filtergram as a function of spatial scale (grey plus symbols). The black cross symbols represent average values of the difference in bins of $0''.05$ with the vertical bars denoting the *rms* value.

Instrumental Stray Light: The blue continuum filtergrams were corrected for instrumental stray light using the PSF (Point Spread Function) described by Mathew et al. (2009). This PSF was derived from transit observations of Mercury on November 8, 2006. Mathew et al. (2009) showed that the removal of stray light renders an improvement in the contrast of bright points in the quiet Sun by a factor of 2.4-2.75 at 430 nm. As the transit observations were taken close to disc center, the same PSF was utilized for removing stray light in the blue continuum filtergrams. The PSF is a weighted linear combination of 4 Gaussians (see Table 1 of Mathew et al. 2009). The deconvolution is carried out using an IDL maximum likelihood routine⁶ (Richardson 1972; Lucy 1974). The method uses the instrument PSF to iteratively update the current estimate of the image by the product of the previous deconvolution and the correlation between re-convolution of the subsequent image and the PSF. The algorithm can be expressed as follows:

$$I = O * P \quad (1)$$

The Image (I) is a result of the convolution between the Object (O) and the Point Spread Function P . Given I

⁶ Called `Max_Likelihood.pro`, from the `AstroLib` package

and P , the most likely O can be iteratively determined as:

$$O^{t+1} = O^t \cdot \left(\frac{I}{C} * \text{conj}P \right) \quad (2)$$

where $C = O^t * P$ under the assumption of Poisson statistics. Here t refers to the iteration cycle.

The corrected and uncorrected sequences were subsequently normalized to the QS intensity. Figure 2 shows a typical scatter plot of intensities in a corrected filtergram and the corresponding uncorrected image. Following stray light correction, the minimum umbral intensity corresponding to the dark umbral core, reduces from $0.1I_{\text{QS}}$ to $0.05I_{\text{QS}}$ which is above the estimated noise level in the the filtergrams. In addition, the fraction of pixels in the umbra having an intensity less than $0.3I_{\text{QS}}$ in both sets of images is $\approx 93\%$. The removal of stray light decreases the mean umbral intensity from $0.202I_{\text{QS}}$ to $0.167I_{\text{QS}}$ while the *rms* contrast increases from 0.059 to 0.086 which is a factor of 1.45. The middle and bottom panels of Figure 3 show the uncorrected and corrected image respectively. The umbral region is extracted from the sunspot shown as the contoured region (top panel of Figure 3). The stray light corrected image exhibits various fine scale features which are described in the following section. Hereafter ‘uncorrected’ and ‘corrected’ will be referred to as UN and CR respectively ⁷.

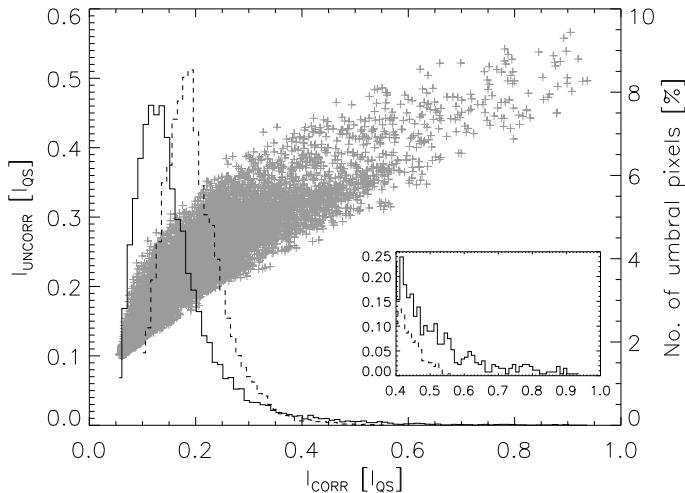


FIG. 2.— Change in umbral intensity after removal of stray light. Displayed is a scatter plot of uncorrected (I_{uncorr}) and corrected (I_{corr}) blue continuum intensity in the umbra. Note that the axes are scaled differently. The *solid* and *dashed* lines refer to the intensity histograms of the corrected and uncorrected filtergrams respectively with a binsize of $0.01I_{\text{QS}}$. A magnified version of the trailing halves of the histograms is shown in the inset.

3. RESULTS

3.1. Umbral Fine Structure

(a) *Short Filaments*: Figure 3 depicts three examples of short filaments (shown in *dashed circles*) near the periphery of the umbra that closely resemble penumbral filaments. These short structures have varying lengths with a dark lane and two adjacent brightenings, and a

⁷ The movie of the uncorrected and corrected images is available at www.prl.res.in/~eugene/movie-umbral-dots.wmv

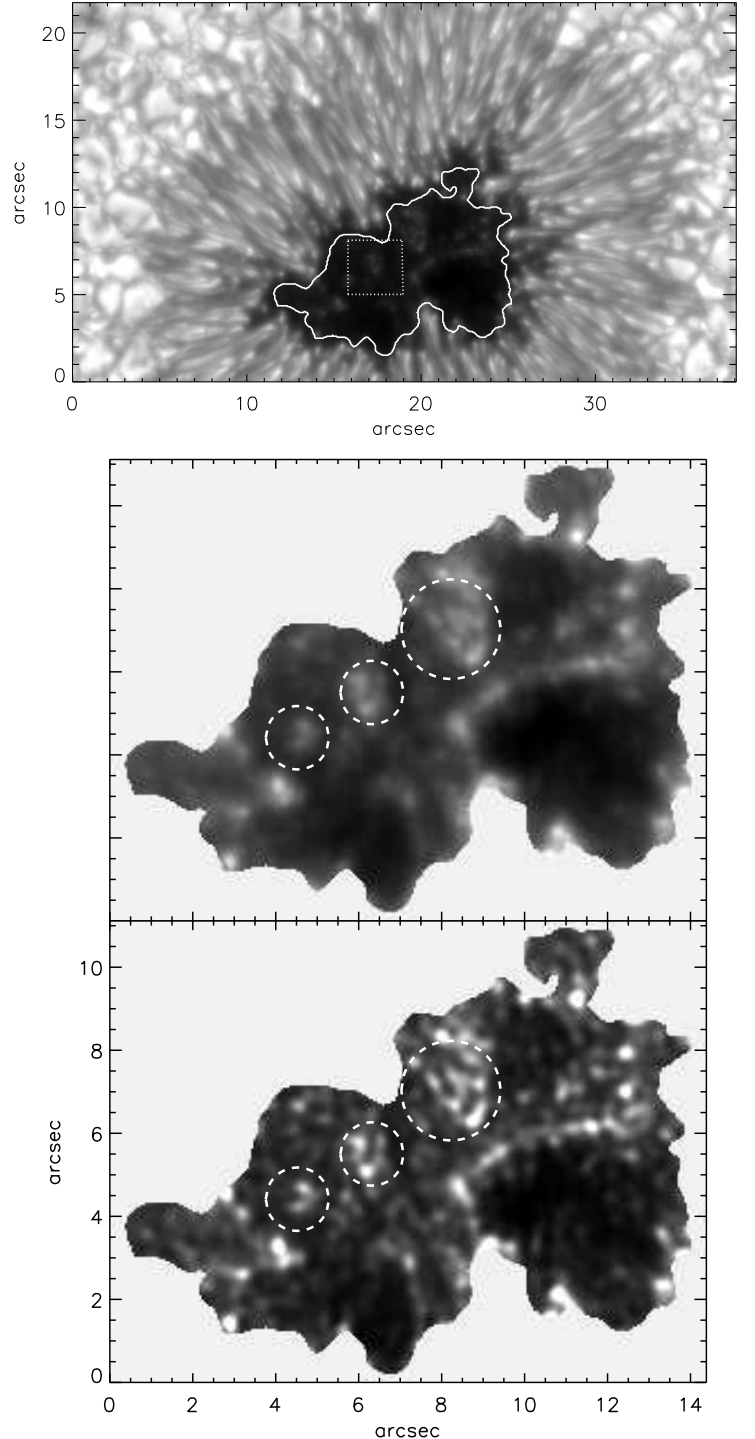


FIG. 3.— Improvement in image contrast after removal of stray light. **Top**: Sunspot in NOAA AR 10944. The white contour refers to the umbral area chosen for analysis. The *dotted white* box represents a selected field-of-view shown in Figure 4. **Middle**: Magnified view of umbra before stray light correction. **Bottom**: Stray light corrected image. The images in the middle and bottom panels have been scaled identically. The *white dashed* circles enclose short filaments that are described in Section 3.1.

bead-like brightening at the tip of the filament facing the umbra. The width of the filaments shown in the figure range from 165 - 200 km where the latter can be considered an upper limit for these structures. These dark filaments are similar to the ones reported by Rimmele (2008); Sobotka & Puschmann (2009) and in numerical

simulations (Rempel et al. 2009b). However, to the best of our knowledge this is the first time that such filaments have been seen in *Hinode* observations. Their morphology is different from the traditional dark lane associated with UDs as observed by Rimmele (2008); Sobotka & Puschmann (2009) and Ortiz et al. (2010). The filament indicated by the largest circle in the bottom panel of Figure 3 partially obscures a neighboring filament to its right.

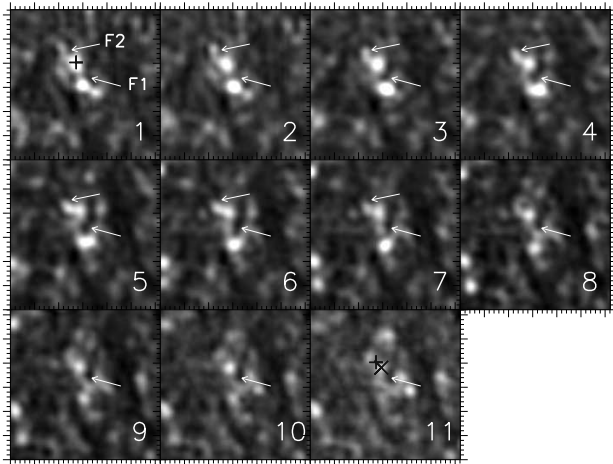


FIG. 4.— Temporal evolution of dark filaments and umbral dots. The images correspond to the field-of-view indicated by the *dotted white* box in Figure 3. The frames have a cadence of 100s and show an UD traveling from the end of one dark filament F2 to the flank of another filament F1. The *black plus* and *cross* symbols denote the initial and final position of the UD in the time sequence respectively. Each major tickmark corresponds to $0''.5$.

Figure 4 depicts the temporal evolution of a set of dark filaments and bright UDs. One can identify at least two main filaments labeled F1 and F2. The time separation between individual frames is 100 s. The lifetime of F1 and F2 is estimated to be 18 and 10 min respectively. These values can be regarded as lower limits since both of them were present from the start of the sequence. The *black plus* symbol marks the position of a bright grain/UD which is seen during the chosen sequence. The UD starts at the end of F2 and ends adjacent to F1 on its left. The total displacement of the UD from frame 1 to 11 (cross symbol) is $\sim 0''.15$ for the 18 min sequence. In general, these localized brightenings/UDs move from the tip/end of one filament onto the flank of another. This motion is continued till they can no longer be distinguished from the background. The dark filaments usually maintain their form during the motion of the UDs after which they can either diffuse or break up into even smaller dark segments.

(b) *Light Bridges*: In addition to UDs, sunspot umbrae often exhibit light bridges (LBs). These can be broadly classified into two categories, namely - strong and faint (Sobotka et al. 1993, 1994). While the former split the umbra into individual cores and represent an abrupt change in the umbral morphology, the latter are usually less than $1''$ in width and are composed of a chain of UDs. The top panel of Figure 3 shows the umbra to be devoid of any large scale structuring, but Figure 5 indicates a faint LB near the right-hand side of the umbra, that is nearly horizontally orientated above an umbral

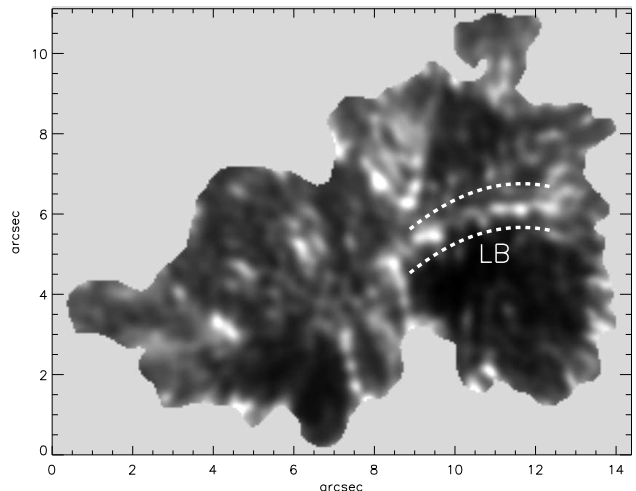


FIG. 5.— Average image constructed from 120 frames in the stray light corrected sequence with the white *dashed* lines indicating a faint light bridge.

dark core. The image is an average of 120 filtergrams covering a 50 min duration. The LB consists of several bright grains resembling UDs whose width is $\approx 0''.23$ and is close to the resolution limit of *Hinode*. The average grain spacing on the LB is estimated to be $0''.25$ while the length of the LB is nearly $3.8''$.

3.2. Properties of UDs

This section describes the physical properties of UDs which were determined from the time sequence of the uncorrected as well as corrected blue continuum image sequences. Identifying and tracking of UDs involves the following steps—

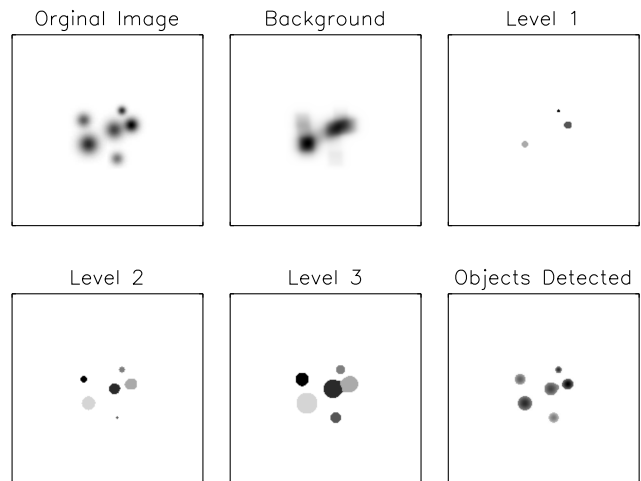


FIG. 6.— Depiction of MLT algorithm for 3 intensity levels. The original image comprises of an arbitrary distribution of intensities. The maximum and minimum intensity range is split into 3 intermediate levels and the objects are sequentially tagged from the highest to the lowest level. The object boundary is determined using the background image from which the features can be isolated as shown in the bottom right panel.

1. *Defining the umbra-penumbral boundary*: The sequence of corrected images are added to obtain a mean image. After smoothing the mean image

using a 11×11 pixel boxcar, the umbra-penumbra boundary is defined by a single continuous contour corresponding to an intensity of $0.3I_{QS}$. This contour is used to construct a binary mask which allowed us to extract the umbral region from individual images.

2. The identification of UDs was carried out using a 2D MLT (Multi Level Tracking; Bovelet & Wiehr 2001) algorithm that has been described by Riethmüller et al. (2008b) for detecting umbral dots. The algorithm identifies objects at different intensity levels starting from the highest level and tagging them uniquely while progressing to lower intensities, till the minimum level is reached. The number of objects (NOs) detected depends on the number of levels (NLs) defined. The latter was chosen by implementing the algorithm for different levels and counting the total NOs detected. For both the UN and CR images, the NOs increase exponentially with the NLs. A non-linear least square fit provided an optimal value of 33 and 25 intensity levels for the UN and CR images respectively. The above values correspond to the knee of the best fit.
3. *Defining the background image:* The thin plate spline technique (Barrodale et al. 1993) was employed to construct the background umbral image, i.e. the intensity distribution in the absence of UDs. Each UD is defined by the intensity contour corresponding to $(I_{\max} + I_{\text{bg}})/2$, where I_{\max} and I_{bg} refer to the maximum/peak and background intensity respectively. Figure 6 depicts the functionality of the algorithm based on 3 levels for an arbitrary distribution of features. For each UD, the following quantities are determined: I_{\max} , I_{bg} , I_{mean} and D_{eff} . The effective diameter D_{eff} expressed in km, is calculated as $\sqrt{4A/\pi}$ where A is the total number of pixels. In addition, the spatial location of the maximum intensity (X_p , Y_p) is also noted. This information is required to track the UDs in the image sequence. Before saving the above information for each UD, the routine also verifies if the UDs are separated from the umbra-penumbra boundary. Only those features which are at least 2 pixels inward from the edge of the umbral mask are saved and considered for analysis. The fraction of objects that did not get filtered using the above criteria is less than 5%.
4. *Tracking the UDs in time:* Each UD is identified in the successive frame if X_p^i , Y_p^i and X_p^{i+1} , Y_p^{i+1} are at the most 1 pixel apart (where i refers to the frame index). The condition of 1 pixel separation is to ensure that the horizontal speed of the UD does not exceed 1.5 km s^{-1} which is obtained from the spatial sampling of $0''.05$ and a cadence of 26 s. If an UD cannot be identified in the current frame the tracking is extended to 2 successive frames. If this also fails, the tracking is terminated.
5. Once tracking is completed, the following additional properties are determined from the UD trajectories: lifetime (T), horizontal speed (V), birth-death distance (L_{bd}) and trajectory length (L_{tj}).

The effective diameter as well as the mean, maximum and ratio of maximum-to-background intensities are averaged over the trajectory of the UD. The horizontal velocity is calculated as the ratio of the trajectory length and the lifetime.

6. Categorizing UDs into peripheral and central is carried out using a second boundary that lies $\approx 0''.8$ inward from the original umbral mask. UDs which originate in between these two contours are labeled as peripheral and the rest as central.

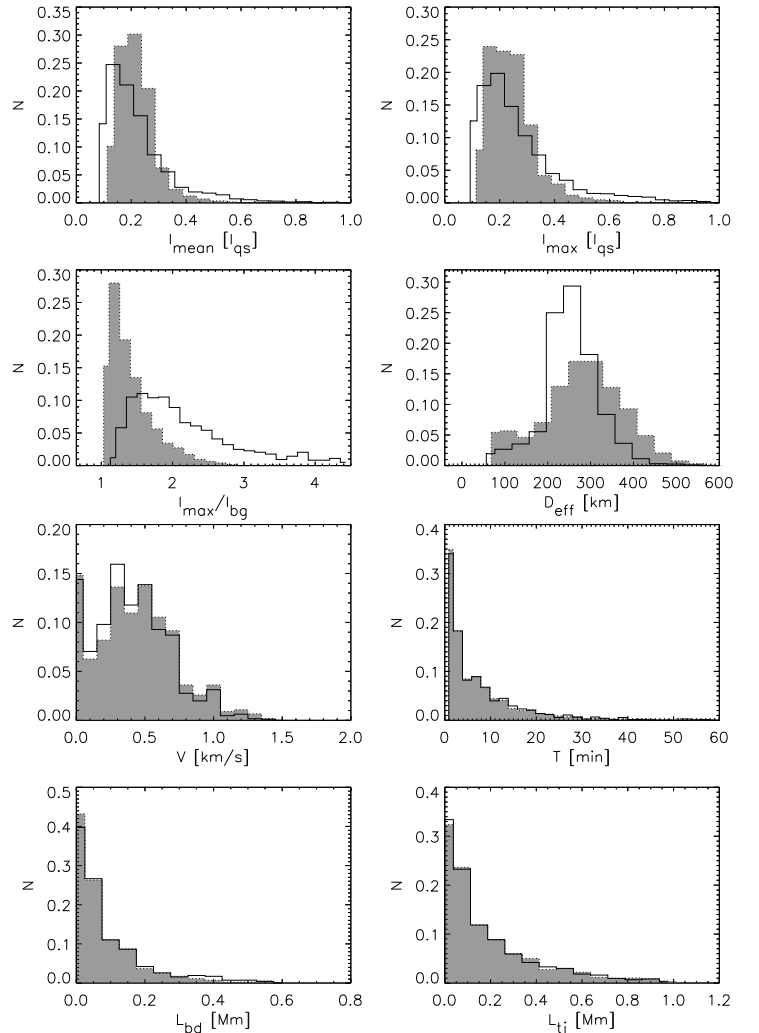


FIG. 7.— Histogram of various UD properties for both time sequences. Mean Intensity - I_{mean} , Maximum Intensity - I_{\max} , maximum-to-background intensity ratio - I_{\max}/I_{bg} , effective Diameter - D_{eff} , horizontal speed - V , lifetime - T , birth-death distance - L_{bd} and trajectory length - L_{tj} . Bin sizes are $0.05I_{QS}$, $0.15I_{QS}$, 0.15 , 40 km , 100 m s^{-1} , 2 min , 50 km , 75 km respectively. The grey shaded and unshaded histograms corresponds to the uncorrected and corrected time sequences respectively. The y -axis represents the fraction of UDs in each bin.

Figure 7 shows the histogram of the various physical properties of all UDs (central and peripheral) whose lifetime exceeds 50 s (2 frames). These UDs constitute $\sim 95\%$ of the total number of objects detected and tracked in both time sequences. The histograms have been normalized to unity for comparison. The bin size

of the quantities corresponding to the UN and CR data is identical. We now turn to the quantitative differences between the physical properties of UD's derived from the uncorrected and corrected sets and whose mean values are summarized in Table 1.

(a) *Intensity*: Removal of stray light produces an extended tail in the histogram while the peak and minimum shift to moderately lower values similar to what was seen in Figure 2. This is more evident in the histogram of peak intensity (I_{\max}). The average value of I_{mean} and I_{\max} are 0.24 and 0.26 I_{QS} respectively for the UN set while the same for the CR sequence are 0.24 and 0.29 I_{QS} respectively. The histogram of I_{mean} peaks at 0.21 and 0.13 I_{QS} for the UN and CR data respectively while for I_{\max} the distribution peaks at 0.16 and 0.19 I_{QS} respectively which is in agreement with Hamedivafa (2011). The maximum intensity of peripheral UD's is on an average 36% greater than that of the central ones after stray light correction.

The distribution of I_{\max}/I_{bg} peaks at 1.18 and 1.58 for the UN and CR sequences respectively. In case of the latter the histogram exhibits a conspicuous tail with I_{\max} being ≈ 4 times greater than I_{bg} for nearly 3% of the UD population. As a result, the estimated mean value of the ratio become 2.5 in comparison to 1.48 in the uncorrected sequence. Such a trend is similar to the area histogram of continuum intensity at 630 nm obtained for numerically simulated UD's (Bharti et al. 2010).

(b) *Size*: Stray light removal reduces the mean effective UD diameter from 295 km to 272 km. The histogram for the latter is narrower and shows a strong peak at 257 km while the former is more broader with a maximum around 288 km. For the corrected sequence, central and peripheral UD's have a mean effective diameter of 298 km and 239 km respectively which is consistent with the findings of Riethmüller et al. (2008b). The sizes of peripheral UD's are smaller than those of central UD's which is similar to that of Riethmüller et al. (2008b). Bharti et al. (2010) state that the average diameter of simulated UD's is ≈ 320 km with the histogram suggesting that UD's do not have a typical size. In comparison, the histograms of the effective diameter shown in Figure 7 and that obtained by Riethmüller et al. (2008b) tend to be nearly symmetrical.

(c) *Horizontal Speed*: Central as well as peripheral UD's tend to be mobile with speeds of ≈ 510 and 460 m s^{-1} respectively for the uncorrected set. In the corrected sequence the speeds of central and peripheral UD's tend to be nearly the same, 460 and 440 m s^{-1} , respectively, which is in good agreement with Kilcik et al. (2012). Riethmüller et al. (2008b) find peripheral UD's to be faster than central ones by 40 m s^{-1} while Watanabe et al. (2009) report a difference of 170 m s^{-1} . Although the above values show peripheral UD's to be slower than central UD's, the maximum speed of the former is nearly 200 m s^{-1} greater than the latter. In addition, the difference in the value is small compared to the spread in the distribution. The reduced speed of peripheral UD's in our case could be attributed to the umbral region defined by the mask described earlier. Nearly 15% of the population tend to be stationary in

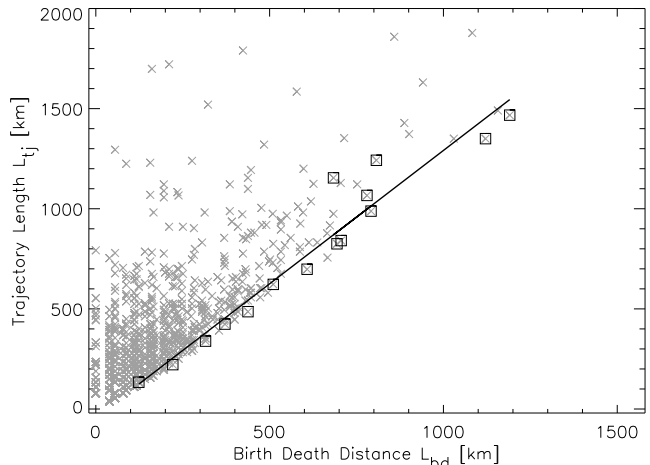


FIG. 8.— Relation between L_{bd} and L_{tj} . The scatter plot between birth-death distance and trajectory length shown as grey cross symbols. The square symbols represent maximum L_{bd} for a given L_{tj} within a bin of 100 km. The straight line is a linear fit to the scatter of the square symbols.

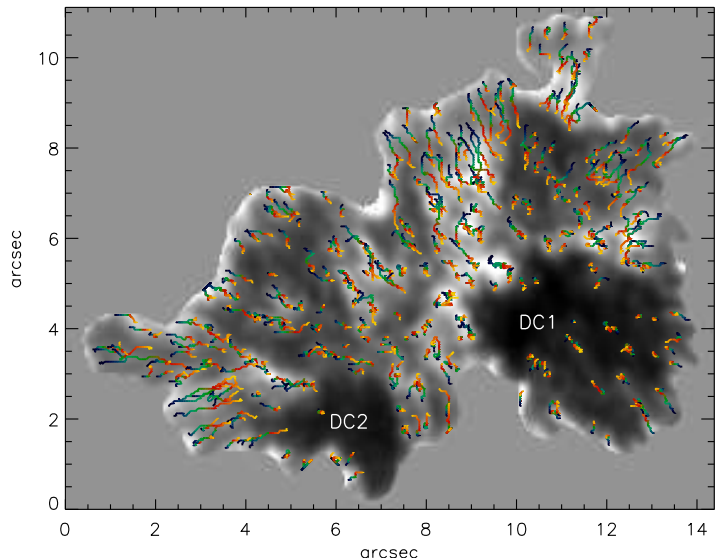


FIG. 9.— Trajectories of UD's. The trajectory of UD's is overlaid on the time average image from the stray light corrected sequence. Blue and yellow represent birth and death respectively. Only UD's whose lifetime exceeds 10 min have been shown in the figure. DC1 and DC2 refer to the two strong dark cores in the umbra.

both sequences. Figure 7 shows that the overall trend of the histograms for the UN and CR sets are quite similar with some minor differences in the leading half of the distribution.

(d) *Lifetimes*: UD's do not exhibit a typical lifetime as is evident from Figure 7 (second column third row). The distribution is exponential with the peak coinciding with the smallest lifetime bin. With a cutoff of 75 s, our analysis puts the mean value of central and peripheral UD's at 8.9 and 7.8 min respectively for the corrected image sequence. This is consistent with lifetimes obtained by Hamedivafa (2008) and Riethmüller et al. (2008b). According to Hamedivafa (2011), who obtained a similar exponential distribution, central and peripheral UD's have a typical half-life of 5 and 3 min respectively while Watanabe et al.

TABLE 1
MEAN VALUE OF PHYSICAL PROPERTIES OF UDS AVERAGED OVER THEIR TRAJECTORIES ALONG WITH THEIR *rms* VALUE. THE NUMBERS IN THE PARANTHESES DENOTE THE NUMBER OF UDS IN THAT GROUP.

Parameter	All UDs		Central UDs		Peripheral UDs	
	No Stray Corr. (1690)	With Stray Corr. (1949)	No Stray Corr. (953)	With Stray Corr. (1096)	No Stray Corr. (737)	With Stray Corr. (853)
$I_{\text{mean}} (I_{\text{QS}})$	0.24±0.07	0.24±0.13	0.21±0.05	0.21±0.09	0.27±0.08	0.28±0.16
$I_{\text{max}} (I_{\text{QS}})$	0.26±0.09	0.29±0.17	0.23±0.06	0.25±0.12	0.30±0.10	0.34±0.21
$I_{\text{max}}/I_{\text{bg}}$	1.48±0.34	2.50±1.26	1.43±0.28	2.33±0.91	1.54±0.39	2.72±1.57
D_{eff} (km)	295±101	272±68.0	337±81.0	298±54.0	241±98.0	239±69.0
V (km s ⁻¹)	0.49±0.35	0.45±0.32	0.51±0.36	0.46±0.32	0.46±0.33	0.44±0.32
T (min)	8.80±11.9	8.40±10.5	7.10±8.70	8.90±11.7	10.9±14.7	7.80±8.70
L_{bd} (km)	94.±120	112±144	90.±109	109±143	100±133	115±145
L_{tj} (km)	240±314	221±283	215±271	233±309	271±360	206±245

(2009) report moderately smaller lifetimes of 6.5 and 7.8 min respectively. These values however are much smaller than the ones obtained by Bharti et al. (2010) who report mean values of ≈ 25 min for simulated UDs. UDs which are present at the begininng or at the end of the time series constitute only 5% of the total number and do not influence the lifetime histogram.

(e) *Trajectory*: The bottom panels of Figure 7 correspond to the birth-death distance and trajectory length of UDs respectively. The overall distribution of the above quantities appear quite similar in both image sequences.

Nearly 55% of the UD population have trajectory lengths of less than 150 km and mean horizontal speeds of 375 m s⁻¹. By comparison, the rest of the group are relatively mobile with speeds of 550 m s⁻¹. The relation between L_{tj} and L_{bd} shown in Figure 8, illustrates that for a given trajectory length there exists a range of birth-death distances. However, the maximum value of L_{bd} varies linearly for any L_{tj} or even when the latter is averaged within a certain length range. The linear relation is shown for the square symbols which correspond to the maximum birth-death distance for a given trajectory length within bins of 100 km.

The trajectories of UDs from their point of origin to death is shown in Figure 9. These paths have been overlaid on the time averaged image from the stray light corrected sequence. The figure only shows the trajectories of those UDs whose lifetime exceeds 10 min. These features constitute 23% of the UD population. Peripheral UDs have a tendency to move inward into the umbra with a nearly linear trajectory. At least two strong dark cores can be identified in the umbra which have been labeled DC1 and DC2 in the figure. One finds that UDs tend to gather or terminate near the edges of these dark cores which is qualitatively in agreement with Watanabe et al. (2009). Furthermore, there does not appear to be a strict segregation of the nature of trajectories on the basis of the location/origin of UDs. For instance, UDs with nearly linear radial tracks are not necessarily confined to the periphery of the umbra while those with squiggly trajectories having birth-death distances less than 200 km are mostly located in the inner regions of the umbra. The latter are observed particularly in the bright parts of the umbra including the region between DC1 and DC2 as well as the light bridge on the northern boundary of

DC1.

TABLE 2
LINEAR CORRELATION COEFFICIENTS (CCs) BETWEEN VARIOUS PROPERTIES FOR ALL, CENTRAL AND PERIPHERAL UDS. THE VALUES SHOWN IN THE TABLE CORRESPOND TO THE UNCORRECTED SEQUENCE WHILE THOSE IN PARANTHESES REPRESENT CORRELATIONS FROM THE STRAY LIGHT CORRECTED SET. CCs GREATER THAN 0.3 ARE SHOWN IN BOLDFACE.

Correlation between	All UDs	Central	Peripheral
$I_{\text{max}} - V$	-0.06(-0.004)	-0.04(0.01)	-0.01(0.01)
$I_{\text{max}} - L_{\text{bd}}$	0.24(0.31)	0.35(0.45)	0.20(0.25)
$I_{\text{max}} - L_{\text{tj}}$	0.25(0.27)	0.30(0.39)	0.22(0.25)
$I_{\text{max}} - T$	0.33(0.28)	0.34(0.38)	0.30(0.29)
$D_{\text{eff}} - V$	0.21(0.20)	0.09(0.13)	0.27(0.26)
$D_{\text{eff}} - T$	-0.08(-0.04)	0.27(-0.13)	-0.18(-0.06)
$D_{\text{eff}} - L_{\text{bd}}$	0.21(0.02)	0.16(-0.16)	0.31(0.16)
$D_{\text{eff}} - L_{\text{tj}}$	0.04(0.03)	0.28(-0.10)	-0.05(0.08)
$V - L_{\text{tj}}$	0.25(0.23)	0.23(0.17)	0.27(0.33)
$T - L_{\text{tj}}$	0.86(0.89)	0.90(0.91)	0.84(0.86)
$T - V$	-0.03(-0.02)	-0.01(-0.05)	-0.03(0.02)

Table 2 lists the linear correlation coefficients (CCs) between various properties for both uncorrected and corrected sequences (values within parantheses for the latter). The CCs are calculated between V , T , L_{bd} as well as L_{tj} with I_{max} and D_{eff} . CCs greater than 0.3 are shown in boldface. The peak intensity of UDs is poorly correlated with its horizontal speed. If one considers the correlation between the peak intensity at the point of emergence with the average velocity (total distance/total time), there is no substantial change from the values cited in the table. Brighter, central UDs have larger birth-death distances as well as trajectory lengths as indicated by the moderate CC which is seen in both the uncorrected and corrected sets. However, the CC worsens in the case of peripheral UDs which tends to bring down the same for the entire sample of UDs.

Brighter UDs also tend to be long lived with values of 0.38 and 0.29 for central and peripheral UDs, respectively, as derived from the corrected sequence. A modest correlation between size and speed is observed predominantly in peripheral UDs. In addition larger UDs of either kind do not show any preference with lifetimes,

birth-death distances and trajectory lengths resulting from the corrected images. The same is the case for the uncorrected images with the exception of a weak correlation between size and birth-death distance for peripheral UDs. In comparison to central UDs, peripheral UDs exhibit a better, although moderate, correlation between mobility and trajectory lengths. The lifetimes on the other hand, are strongly correlated with trajectory lengths. This trend is expected since the trajectory length is dependent on the number of frames for which the feature is tracked. The lifetime of UDs is poorly correlated with its horizontal speed.

3.3. Spatial and Temporal Coincidence

The time sequence movie reveals that UDs tend to move along trajectories that are traced by subsequent UDs. This would suggest that there are regions/pockets in the umbra which favor the emergence and disappearance of UDs. There could also exist a time delay or a set of delays between the appearance of one UD and the emergence/disappearance of another at the same spatial location. This aspect is dealt with in the following manner. From the information table of each UD, one can extract the time interval between the i) birth of two UDs, ii) birth of one UD with the death of another and vice-versa and iii) death of two UDs, where all three classes of events refer to the same spatial location. These events can be referred to as birth-birth (BB), birth-death-birth (BDB) and death-death (DD) respectively. We confine our analysis and discussion to central UDs, since the origin of peripheral UDs is predominantly in the penumbra (Sobotka & Jurcak 2009a; Watanabe et al. 2009).

The top panel of Figure 10 shows the distribution of the number of events in the three classes respectively for all UDs whose lifetime exceeds 150 s. The histograms indicate that there is no unique time lag between successive events in either class, although BDB and DD have a tendency to have shorter time delays than the BB class. Mean time delays of 45.5, 52.0 and 49.8 min were estimated for the three classes respectively. If the minimum lifetime of the UDs is varied in the range 50s - 10 min, the mean value of the distribution in all three event classes are limited within ± 5 min of the above values. Taking the average time delay for this range of lifetimes, one obtains 46, 53 and 47 min for the each event class respectively. By comparison, the number of events in BB are fewer than the other two for any given minimum lifetime. However, for short lived UDs ($T < 150$ s), the number of BB and DD events are comparable with mean time delays of 45, 46 and 52 min in the three classes respectively.

The bottom panel of Figure 10 shows the spatial distribution of the occurrences of all three event classes which are indicated by the *plus*, *triangle* and *cross* symbols respectively. The color corresponds to the normalized time delay associated with that spatial location for each event class. The figure indicates that the pockets of sustained emergence as well as disappearance are scattered everywhere in the umbra with no specific pattern in the distribution. The figure also shows that a particular spatial location is not limited to the event class as at least 12 and 20 instances were estimated to be common to BB and BDB as well as BDB and DD respectively. While a similar characteristic of spatial coincidence of inter event classes is seen for UDs with lifetimes of less than 2 min,

the number of coincidences is higher namely, 19 cases each for the above two inter event classes. This would suggest that short lived UDs tend to reappear or emerge from the point of disappearance of former UDs.

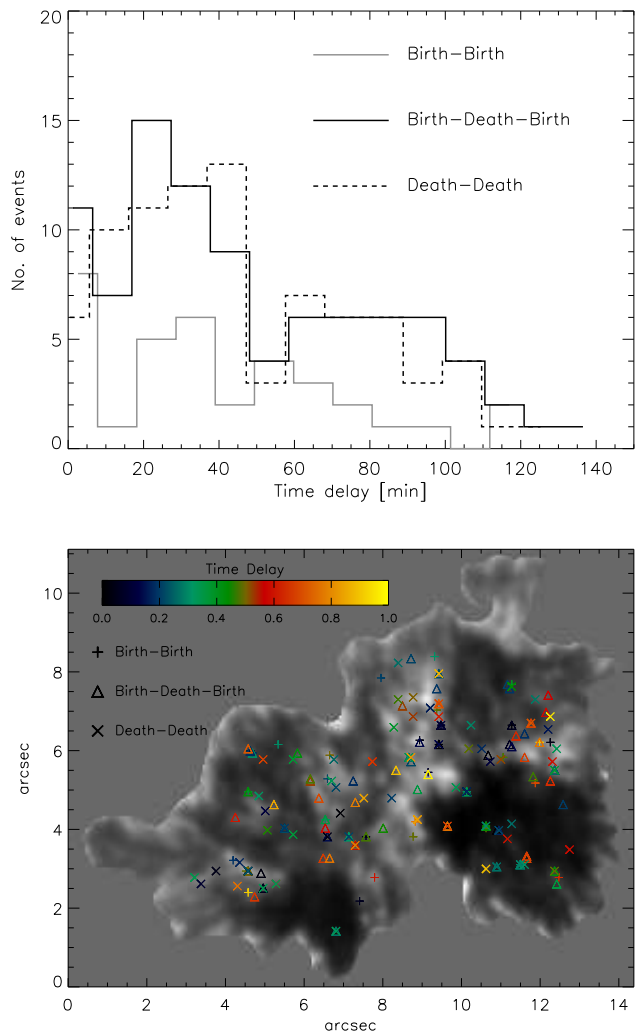


FIG. 10.— **Top:** Histograms of time delays associated with each event class: BB—(grey), BDB—(solid black), DD—(black dotted). **Bottom:** Spatial distribution of the occurrences of all three event classes (see text) which are indicated by the *plus*, *triangle* and *cross* symbols respectively. The color coding indicates the normalized time delay associated with that spatial location for each event class. BB:Birth-Birth, BDB:Birth-Death-Birth, DD:Death-Death.

4. SUMMARY AND DISCUSSION

We employ a 2 hr 20 min time sequence of high resolution blue continuum filtergrams of the sunspot in NOAA AR 10944 from *Hinode* SOT to determine the properties of umbral dots and analyze the umbral fine structure after careful removal of instrumental stray light. The motivation of our study stems from the fact that stray light reduces image contrast which could influence the photometric and geometric properties of umbral features. After deconvolving the filtergrams with an instrumental PSF, whose wings describe the scattered light in the telescope, we find that the *rms* contrast of the images increases by a factor of 1.45. In addition, the mean umbral intensity decreases by $\approx 17\%$.

TABLE 3
COMPARISON OF A FEW PHYSICAL PROPERTIES OBTAINED PREVIOUSLY FROM *Hinode*, GROUND-BASED OBSERVATIONS AND NUMERICAL SIMULATIONS.

Reference	Source	UD Identification Algorithm	D_{eff} (km)	$I_{\text{max}}/I_{\text{bg}}$	V (km s $^{-1}$)	T (min)
No Stray Light Correction	<i>Hinode</i>	MLT	295±101	1.48±0.34	0.49±0.35	8.8±11.9
Watanabe et al. (2009)	<i>Hinode</i>	Intensity Thresholding	184	1.73	0.44	7.35
With Stray Light Correction	<i>Hinode</i>	MLT	272±68	2.50±1.26	0.45±0.32	8.4±10.5
Hamedivafa (2008)	0.5 m SVST	Low-Noise Curvature Detection	230	–	<1.0	7-10
Riethmüller et al. (2008b)	1.0 m SST	MLT	272±53	1.17±0.1	0.42±0.20	10.5±10.5
Sobotka & Puschmann (2009)	1.0 m SST	Low-Noise Curvature Detection	125	2.4	0.34	9.1
Kilcik et al. (2012)	1.6 m NST	Area & Intensity Thresholding	254	–	0.45	8.19
Rempel et al. (2009a)	Simulations	Area & Intensity Thresholding	295	–	0.35	12.9
Bharti et al. (2010)	Simulations	MLT	420	2.88	–	25.1

With scattered light accounted for, one is able to identify short filamentary structures resembling penumbrae but well separated from the umbra-penumbra boundary. The features consist of a dark filament with bright filaments/grains adjacent to it. The width of the dark filament is at the resolution limit of *Hinode*, suggesting that these structures are largely unresolved. Their lifetimes are of the order of 10-20 min during which bright grains can transit from one filament to another remaining close to the dark filament. The existence of similar features have already been reported by Rimmele (2008); Sobotka & Puschmann (2009) based on ground based observations from larger telescopes as well as from numerical simulations (Rempel et al. 2009b). We however, do not find sub-structures in UD's namely, the dark lanes, which represent hot convective plumes, since they are still below the detection capability of *Hinode*. The observations of Bharti et al. (2007) are reminiscent of fragmenting light bridges that often exhibit dark cores along their axis (Lites et al. 2004; Rimmele 2008; Louis et al. 2008).

Various physical properties of umbral dots were determined after they were identified in individual images and tracked in time. To that end, a multi-level tracking algorithm was applied to both the uncorrected and corrected image sequences. The following properties were analyzed : mean intensity (I_{mean}), maximum intensity (I_{max}), ratio of maximum-to-background intensity ($I_{\text{max}}/I_{\text{bg}}$), effective diameter (D_{eff}), horizontal speed (V), lifetime (T), birth-death distance (L_{bd}) and trajectory length (L_{tj}). The mean value of the above quantities derived from the stray light corrected image sequence are $0.24I_{\text{QS}}$, $0.29I_{\text{QS}}$, 2.5, 272 km, 0.45 km s $^{-1}$, 8.4 min, 112 km and 221 km respectively. The distribution of the values describing the photometric and geometric properties is more strongly affected by the presence of stray light while it is less severe in the case of the kinematic parameters.

The time sequence of corrected images was also used to determine if umbral dots prefer to appear or disappear at specific locations in the umbra. Furthermore, any specific time delay or a set of time delays associated with subsequent emergence/disappearance was also determined. The events which were sorted as birth-birth, birth-death-birth and death-death do not have a unique time delay with a majority of events in either group having a value varying between 45-50 min. These values are also insensitive to the minimum lifetime of umbral dots. The spatial locations where these events occur are scat-

tered in the umbra and in general do not highlight a specific pattern. In addition, there are several pixels where events from either class can overlap. This would suggest that umbral dots tend to reappear or emerge from the location of disappearance of former umbral dots.

Table 3 gives mean values of a few properties obtained previously from *Hinode*, ground-based observations and numerical simulations. The values obtained from the uncorrected sequence are in good agreement with those reported by Watanabe et al. (2009) for the same data set described in this paper, although they employed a different identification routine. On the other hand, the corresponding values obtained from the stray light corrected images are consistent with Hamedivafa (2008); Riethmüller et al. (2008b); Kilcik et al. (2012). The ratio of maximum-to-background intensity ($I_{\text{max}}/I_{\text{bg}}$) is particularly in good agreement with those obtained by Sobotka & Puschmann (2009) and Bharti et al. (2010). There appears to be some differences between the results derived from numerical simulations by Rempel et al. (2009a) and Bharti et al. (2010) which show UD's to be larger, slower and long-lived than those retrieved from observations. The deviations between the two sets of simulations could be attributed to the boundary conditions and treatment of numerical diffusivities (Kilcik et al. 2012). In the case of observations, there is general consensus that UD's are typically 250 km in diameter and have lifetimes of 10 min and horizontal speeds of 450 m s $^{-1}$. Another point of disagreement between simulations and observations is the ubiquitous presence of UD's in the former that do not give any indication of structuring in the umbra, i.e. faint light bridges and umbral dark cores.

With the exception of intensity vs diameter, none of the UD properties are well correlated with each other (Kilcik et al. 2012). In simulations, the correlation coefficient is nearly 0.6 but can vary between 0.02 and 0.3 depending on the sample of UD's taken from relatively bright locations in the umbra (Kilcik et al. 2012). The monotonicity seen in simulations, exists with a significant scatter between the intensity and diameter of UD's. The differences between observations and simulations, needs to be addressed with complementary polarimetric observations at high spatial resolution (<0".15) which could provide additional constraints for MHD models. This is necessary for determining the physical mechanisms driving UD's and their kinematics, for which instruments such as the CRISP (Scharmer et al. 2008) and the GFPI (Gre-

gor Fabry-Pérot Interferometer; Denker et al. 2010) will be crucial.

Our sincere thanks to the *Hinode* team for providing the data used in this paper. *Hinode* is a Japanese mission developed and launched by ISAS/JAXA, with NAOJ as domestic partner and NASA and STFC (UK) as international partners. It is operated by these agencies in

co-operation with ESA and NSC (Norway). The authors thankfully acknowledge the comments and suggestions of the referee. Our work has been partially funded by the Spanish MICINN through projects AYA2011-29833-C06-04 and PCI2006-A7-0624, and by Junta de Andalucía through project P07-TEP-2687, including a percentage from European FEDER funds.

REFERENCES

- Barrodale, I., Skea, D., Berkley, M., Kuwahara, R., Poekert, R. 1993, *Pattern Recognition*, 26, 375
- Bharti, L., Joshi, C., Jaaffrey, S. N. A. 2007, *ApJ*, 669, L57
- Bharti, L., Beeck, B., Schüssler, M. 2010, *A&A*, 510, A12
- Bovelet, B., Wiehr, E. 2001, *Sol. Phys.*, 201, 13
- Denker, C. Balthasar, H., Hofmann, A., Bello González, N., Volkmer, R. 2010, in *Ground-based and Airborne Instrumentation for Astronomy III*, ed. I. McLean, S. Ramsay & H. Takami, *SPIE Conf. Ser.*, 7735
- Hamedivafa, H. 2008, *Sol. Phys.*, 250, 17
- Hamedivafa, H. 2011, *Sol. Phys.*, 270, 75
- Hartkorn, K., Rimmele, T. 2003, *ASPC*, 286, 281
- Kitai, R., Watanabe, H., Nakamura, T., Otsuji, K., Matsumoto, T., Ueno, S., Nagata, S., Shibata, K., Muller, R., Ichimoto, K., Tsuneta, S., Suematsu, Y., Katsukawa, Y., Shimizu, T., Tarbell, T. D., Shine, R. A., Title, A. M., Lites, B. W. 2007, *PASJ*, 59, S585
- Kilcik, A., Yurchyshyn, V. B., Rempel, M., Abramenko, V., Kitai, R., Goode, P. R., Cao, W., Watanabe, H. 2012, *ApJ*, 745, 163
- Kosugi, T., Matsuzaki, K., Sakao, T., Shimizu, T., Sone, Y., Tachikawa, S., Hashimoto, T., Minesugi, K., Ohnishi, A., Yamada, T., Tsuneta, S., Hara, H., Ichimoto, K., Suematsu, Y., Shimojo, M., Watanabe, T., et al. 2007, *Sol. Phys.*, 243, 3
- Lites, B. W., Scharmer, G. B., Berger, T. E., Title, A. M. 2004, *Sol. Phys.*, 221, 65
- Louis, R. E., Bayanna, A. R., Mathew, S. K., Venkatakrisnan, P. 2008, *Sol. Phys.*, 252, 43
- Lucy, L. B. 1974, *AJ*, 79, 745
- Mathew, S. K., Zakharov, V., Solanki, S. K. 2009, *A&A*, 501, L19
- Ortiz, A., Bellot Rubio, L. R., van der Voort, L. R. 2010, *A&A*, 713, 1282
- Parker, E. N. 1979, *ApJ*, 234, 333
- Rempel, M., Schüssler, M., Cameron, R. H., Knölker, M. 2009a, *Science* 325, 171
- Rempel, M., Schüssler, M., Knölker, M. 2009b, *ApJ*, 691, 640
- Richardson, W. H. 1972, *J. Opt. Soc. Am.*, 62, 55
- Rimmele, T. R. 2004, *ApJ*, 604, 906
- Rimmele, T. 2008, *ApJ*, 672, 684
- Riethmüller, T. L., Solanki, S. K., Lagg, A. 2008a, *ApJ*, 678, L157
- Riethmüller, T. L., Solanki, S. K., Zakharov, V., Gandorfer, A. 2008b, *A&A*, 492, 233
- Scharmer, G. B., Narayan, G., Hillberg, T., de la Cruz Rodriguez, J., Löfdahl, M. G., Kiselman, D., Sütterlin, P., van Noort, M., Lagg, A. 2008, 689, L69
- Schüssler, M., Vögler, A. 2006, *ApJ*, 641, L73
- Schmidt, W., Balthasar, H. 1994, *A&A*, 283, 241
- Sobotka, M., Bonet, J. A., Vázquez, M. 1993, *A&A*, 415, 832
- Sobotka, M., Bonet, J. A., Vázquez, M. 1994, *A&A*, 426, 404
- Sobotka, M., Brandt, P. N., Simon, G. W. 1997a, *A&A*, 328, 682
- Sobotka, M., Brandt, P. N., Simon, G. W. 1997b, *A&A*, 328, 689
- Sobotka, M., Jurčák, J. 2009a, *ApJ*, 694, 1080
- Sobotka, M., Puschmann, K. G. 2009, *A&A*, 504, 575
- Socas-Navarro, H., Martínez Pillet, V., Sobotka, M., Vázquez, M. 2004, *ApJ*, 614, 448
- Tritschler, A., Schmidt, W. 2002, *A&A*, 388, 1048
- Tsuneta, S., Ichimoto, K., Katsukawa, Y., Nagata, S., Otsubo, M., Shimizu, T., Suematsu, Y., Nakagiri, M., Noguchi, M., Tarbell, T., et al. 2008, *Sol. Phys.*, 249, 167
- Watanabe, H., Kitai, R., Ichimoto, K. 2009, *ApJ*, 702, 1048